Highly Compact Linear Variable Filter in the Mid Infrared Region for Acetone Level Monitoring

Simon Chun Kiat Goh, Li Lynn Shiau, Mohamad Shamsul Bin Mohamad, Chengkuo Lee, and Chuan Seng Tan

***Abstract*—Due to the recent rapid industrialization and urbanization across the world, chemicals are released into the environment at an unprecedented rate. Gas sensors, in particular, interferometric based devices represent an important toolkit for air quality monitoring. Amongst different interferometers, linear variable filter (LVF) holds the promise of a fixed optical component that can be operated under various conditions. In this work, oxide pillars were deposited on a [Si-SiO_2] mirror coated wafers. Thick oxide deposition was performed using a low temperature high density chemical vapor process with photoresist as mask to form pillars. By sandwiching two such substrates together, a milli-degree taper angle was formed by a difference in pillar height. The mated normal incidence LVF was demonstrated with an operating range of 0.7 μm, full width half maximum of 230 nm at 3,500 nm and was tested for the presence of acetone vapor. The relationship between transmission intensity and acetone concentration was plotted with a correlation R^2 of 0.972.**

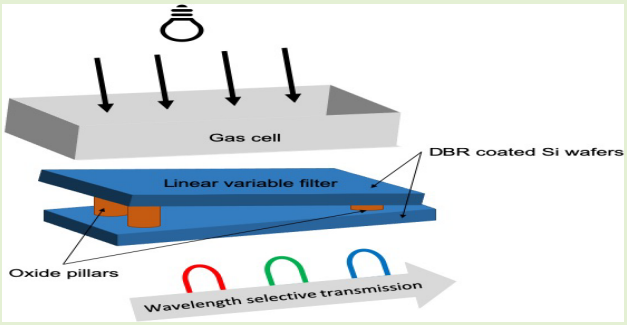

***Index Terms*—Interferometer, Fabry-Perot, linear variable filter, optical sensing, chemical detection, 3DIC, integration, flip chip, silicon photonics.**

I. Introduction

In A world of threats from man-made environmental destructions, ranging from accidental chemical exposure to intentional toxic waste disposal out of convenience, detection tools are becoming a mainstay for many government agencies around the world [1], [2]. Over a span of a few decades, many such tools have been rapidly designed and commissioned for use. These devices include gas chromatography, mass spectrometer, terahertz and optical spectrometers. Until recent years, many of these detectors are bulky, costly and require trained personnel to operate [3]. Today, given the rapid advancement in microfabrication technologies, many of the detectors have been significantly scaled-down in dimensions [4]. The benefits of miniaturized detectors include compactness, low cost, high deployability and remote-sensing possibility due to low power requirement [5], [6]. Amongst the different end uses, many of those sensors have been developed for local air quality monitoring.

In the case of air pollutants, those volatile organic contaminants (VOCs) generally contains hydrocarbon molecules [7], [8]. Some of those VOCs are known to be human carcinogens [9]. So far, a number of different gas sensors for VOCs testing have been demonstrated. These include waveguides [10], partially stripped optical fibres [11], chemo-resistive chemical sensors [12]–[14], photoacoustic spectrometer [15] and refractometer [16]. However, miniaturized packaging of optical fibers is still challenging coupled with the fact that most commercially available fibers are limited to near infrared operation [17]. Chemical based sensors are highly specific to certain molecules. Thus, a collection of different sensors are needed to scan a variety of such VOCs molecules. One main problem is that some of these sensors are effective for single use only. Although photoacoustic spectrometer affords high accuracy in concentration measurement, it requires a highly precise alignment of the laser excitation source which increases production costs. Finally, refractometers, like chemical sensors, are more suit-

Manuscript received October 31, 2019; revised December 14, 2019; accepted December 14, 2019. Date of publication December 25, 2019; date of current version March 17, 2020. This work was supported in part by A*STAR SERC AME Programmatic Fund through Nanosystems at the Edge under Grant A18A4b0055, in part by NRF-CRP15-2015-02 under Grant WBS: R-263-000-C24-281, and in part by A-STAR-NCBR Joint under Grant WBS:R-263-000-C91-305. The associate editor coordinating the review of this article and approving it for publication was Dr. Daniele Tosi. *(Corresponding author: Simon Chun Kiat Goh.)*

Simon Chun Kiat Goh is with the School of Electrical and Electronic Engineering, Nanyang Technological University, Singapore 639798, and also with the Excelitas Technologies, Singapore 627969 (e-mail: gohc0075@e.ntu.edu.sg).

Li Lynn Shiau, Mohamad Shamsul Bin Mohamad, and Chuan Seng Tan are with the School of Electrical and Electronic Engineering, Nanyang Technological University, Singapore 639798 (e-mail: sh0003nn@e.ntu.edu.sg; emohamad@ntu.edu.sg; tancs@ntu.edu.sg).

Chengkuo Lee is with the Department of Electrical and Computing Engineering, National University of Singapore, Singapore 117583 (e-mail: elelc@nus.edu.sg).

Digital Object Identifier 10.1109/JSEN.2019.2962135

able for single analyte concentration monitoring. The addition of other interfering analytes could alter the effective refractive index. On the other hand, on-chip and free-space propagated optical-based spectrometric-enabled sensors have been reported [18]. These non-specific spectrometers could scan a range of wavelength to detect different molecules in the defined spectrum [19]. Subsequently, the obtained spectrum can be compared with those from data libraries for identification of the responsible gas species. Arguably, an optical spectrometric gas sensor is more technologically advanced for elucidating a mixture of known and unknown gas mixture than existing commercially available gas specific sensors.

In particular, interferometric absorption-based optical spectrometers represent an important class of equipment capable of achieving high sensitivity, accuracy and repeatable measurements [20]. During operation, broadband light passes through a medium of analyte. Molecules present in the analytes would absorb a specific spectrum of light with frequency that correspond to the molecule-specific vibrational frequency. Upon excitation, the molecules would perform either stretching, in-plane scissoring, wagging, rocking or twisting motion. Maximum absorption occurs at the molecule resonant frequency. The resonant frequency can be detected by infrared spectroscopy. The response would be reflected as an increase in absorption or a corresponding decrease in transmittance. When the concentration of analyte increases (decreases), more (less) light would be absorbed resulting in the attenuation (intensification) in transmission intensity. The phenomenon can be explained using the Beer-Lambert law which relates the system's absorption characteristics to the presence of absorbing molecules. Notable examples of miniaturized optical spectrometers include Michelson or Fabry-Perot and linear variable filter (LVF) interferometers. Principally, Michelson and Fabry-Perot interferometers are the best-in-class common laboratory-based spectrometers. However, their use as remote sensors is limited by long scan time and their susceptibility to mechanical vibration which distort the output signal. A plausible alternative to Michelson and Fabry-Perot is the LVF. A LVF comprises two fixed mirrors tilted at a tapered angle along the length of the filter [21]. In this case, variable passbands can be obtained at different positions along the filter. While the mirrors determine the range of reflected wavelength, the gap length between the mirrors dictates the passband wavelength.

Unlike a LVF, conventional filters are typically constructed by the deposition of multiple thin film layers to form an interferometric and/or absorbing coating. Specific to gas sensing applications, bandpass filters are generally used to select the absorbing wavelength of a gas species. In this case, one type of chemical would be detected per filter-detector (sensor) setup. So far, a maximum of four channels are typically incorporated into a Transition Outline packaging. This allows a maximum of four different analytes to be detected at any one time. Such products are available commercially. One major challenge is that discrete channel sensors are not able to distinguish between analytes with overlapping absorption peaks properly. As such, additional filters with different bandpass characteristics have to be incorporated onto a platform to form an evenly-spaced wavelength discretized optical sensing device. Although achievable, it is not economical and time consuming for realizing such sensors. In this case, a single LVF coupled with an appropriate linear array detector is sufficient to sweep a range of wavelengths determined by the working range of the filter. Analytes with dissimilar absorption wavelengths could be sensed within the filter working range.

Many mask-free LVF tapers are reportedly made by sputter deposition with a triangle shape opening mask [22]. With translation or rotation, a linearly graduated taper is fabricated [23]. However, this methodology presents the risks of non-uniform taper between sample batches with the same shadow masks in use over time due to clogging [24]. This calls for constant mask replenishment which might incur higher fabrication costs as well as batch to batch fabrication errors. Also, a non-linear taper due to fabrication errors could results in deviated transmission profile. More critically, alterations to LVF profile, as deemed necessary by applications, can only be effected by redesigning the shadow masks.

Various mask-based LVF fabrication approaches have been proposed. Grayscale photomasking has been reported for the formation of the LVF wedge [25]. However, the adoption of grayscale lithography is hampered by the need to acquire expensive photomasks. On the other hand, discrete staircase wedge filter can be fabricated using a number of photomasks and multiple lithography-etching steps to create transmission channels [26]. This method is associated with an increase in the total number of processing steps. Ultimately, the availability of masks limits the total possible number of channels. Also, chemical and/or thermal photoresist reflow technique has been demonstrated for the formation of the wedge profile [27]. The subsequent pattern transfer via substrate etching could result in profile deviation under suboptimal process conditions. This is apparent as the photoresist characteristics change with age, altering the resist to substrate etching ratio. Furthermore, the etching process could introduce rough surface resulting in propagation loss.

In this work, a wafer-level processed LVF is proposed and fabricated. Low-temperature high density chemical vapor deposition (HDCVD) silicon dioxide (SiO_2) pillars were deposited on a distributed Bragg reflector (DBR) coated Si substrate with photoresist as mask. When stacked with a non-pillared DBR-Si, the pillars created a highly linear taper between the two substrates to form a LVF. The proposed LVF affords a simpler and easier methodology to create the taper without the possible constraints imposed by other methods. Moreover, the taper profile can be manipulated by changing the pillar height to tailor the LVF for different application needs. Fabricated LVF were structurally and optically characterized during VOC gas detection between 3.3 and 3.5 μm. By taking the normalized peak transmission intensity, gas concentration can be predicted without strict calibration of the spectrometer.

II. Methodology and Characterization

The fabrication steps are illustrated in Fig 1. Si wafers were cleaned in acetone and isopropanol (IPA) and dried under dry N_2 stream. Thereafter, the wafers were coated with 320 and

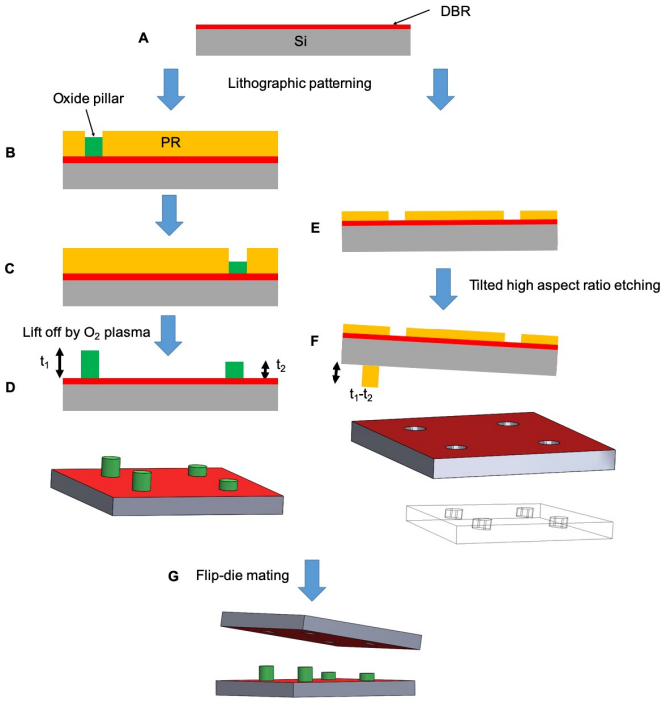

Fig. 1. Shows the fabrication steps. A) Si wafer coated with alternating Si-SiO_2-Si [HLH] thin film as DBR. B) DBR coated Si was lithographically patterned and deposited with SiO_2 ($t = t_1$) followed by PR stripping with O_2 plasma. C) SiO_2 ($t = t_2$) pillars were deposited at another edge of the substrate and then PR stripped. D) Further cleaning (optional) to accomplish different height pillars on the substrate. E) Front side patterning on another DBR-Si substrate. F) Photoresist pillar of height (t_1 - t_2) were backside patterned. Wafer front side was PR patterned was subjected to DRIE. G) Completed (D) and (F) substrates were aligned and mated.

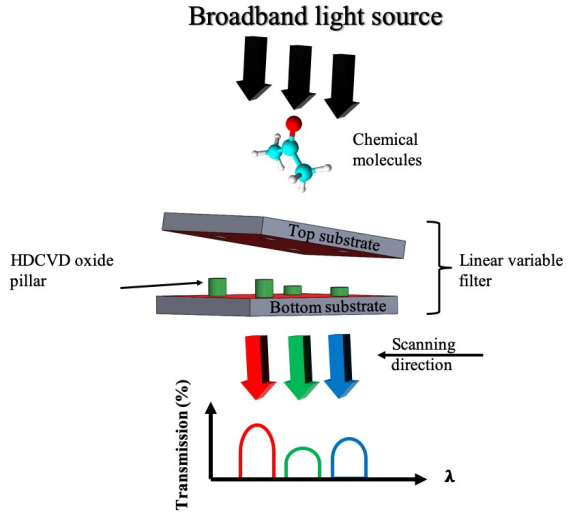

Fig. 2. Illustrates the transmission characteristics of a LVF. The translation along the length of the filter, from shorter to longer resonant gap, will elicit the transmission of shorter to longer wavelength of light, respectively. In the presence of an absorbing molecule, the transmission intensity is attenuation and will be reflected by the linear array detector located beneath the LVF.

770 nm sputtered amorphous silicon [H] and CVD silicon dioxide [L], respectively. In subsequent sections, *[H]* is referenced to a-Si as a high refractive index while *[L]* describes the low refractive index nature of SiO_2. The a-Si - SiO_2 - a-Si DBR, can be referred to [*HLH*]. Thereafter, a wafer was doubly coated with Ma-N 1440 negative photoresist to achieve a total resist height (t_{resist}) of approximately 8 μm. The wafer was then subjected to the first HDCVD SiO_2 deposition. Depending on need, the maximum thickness of SiO_2 (t) is typically taken to be $t_{\text{resist}}/2$ for effective liftoff. The sample chuck temperature was set to 18 °C and the SiO_2 was deposited on one end of the substrate ($t = t_1$) in blocks of 500 nm which required a runtime of 200 s. The resist was then stripped by O_2 plasma. The coating, lithography, deposition and stripping steps were repeated once more on the other end of the substrate ($t = t_2$). On the other wafer, resists corresponding to the difference in thickness between the first and second HDCVD ($t_1 - t_2$) was spin-coated onto both sides of the wafer. The front side was etched for a total of 300 nm using deep reactive ion etching. Subsequently, the first wafer was mechanically diced to dies of dimension 10 mm by 10 mm while the second wafer was diced to the dimension of 8 mm by 5 mm. The dies were then flipped and aligned using a flip-chip bonder to form a LVF. The air gap between the DBR was designed to be the half-wave resonant gap. The presence of liquid or other contaminants, depending on its refractive index, would alter its overall transmission characteristics. It is imperative to keep the gap free from contamination. We envision that the filter-detector setup has to be hermetically sealed using wafer level processing in the future.

Fabricated LVF was characterized using a benchtop Agilent Cary 600 series Fourier transform infrared spectrometer (FTIR) with the onboard microscope. Prior to testing, the aperture of the spectrometer was set to 100 μm x 100 μm. With an unobstructed light path, in the absence of the sample, a background spectrum was acquired in air in transmission mode. A total of 64 scans were obtained. Thereafter, the mated LVF was placed on the sample stage. To obtain good signal response, the sample stage was adjusted until the backside of the LVF top substrate had been focused properly. Thereafter, stepwise signal acquisition at an equal interval of 100 μm was conducted along the length of the filter from the short to the taller end a shown in Fig 2. During each sampling, image focusing is carried out, if necessary, and a total of 64 scans were taken. Atomic force microscopy (AFM) was performed on a Brukers Dimension. A total of 512 lines were obtained with a test area of 100 μm x 100 μm at 1 Hz. Revelation of the oxide pillar cross section was first coated with a strip of Pt layer followed focused ion beam (FIB) milling with Ga ion. Field emission scanning electron microscopy (FESEM) was carried out for visualization at high magnification.

III. Results and Discussion

While designing LVF, Fabry-Perot parallel mirror, as well as Fizeau interferometric models, can be used to approximate the passband position and transmission intensity [28], [29]. Fizeau approximation is generally favored due to its ability to estimate the passband intensity. One disadvantage of the Fabry-Perot model is that it does not account for light "walkaway" effect. Typically, the "walkaway" effect results in transmission intensity loss at longer transmission wavelength. The selection

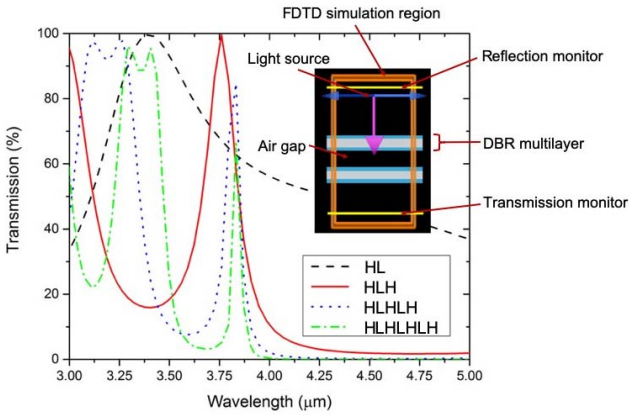

Fig. 3. Shows the transmission characteristics of FDTD simulated Fabry-Perot interferometers with different number of DBR layers. The inset shows the FDTD simulation window with [HLH]- resonant gap – [HLH] configuration.

for whichever model depends largely on design construction. That is, the Fizeau model should be the prime choice when mirror reflectivity (R) is > 95 % and when designed at large propagation mode, $m > 3$ [30].

Principally, the Bragg mirror and resonant gap thicknesses were designed using the quarter-wave (Equation 1) and half-wave stacks (Equation 2) formulae, respectively.

$$t_{H,L} = \frac{m\lambda}{4n} \tag{1}$$

$$t_{gap} = \frac{m\lambda}{2n} \tag{2}$$

where $t_{H,L}$ and t_{gap} refers to the thicknesses of the high (H) and low (L) refractive index thin film and that of the resonant gap, respectively, m refers to the optical propagation mode, n is the refractive index and λ is the center wavelength.

In addition, both sputtered a-Si and SiO_2, as well as the resonant gap (air) thicknesses, were designed at fundamental mode. This concretizes the decision to use FP approximation over that of Fizeau approximation. A simulation was performed using Lumerical FDTD [31]. Due to the fact that it would be near impossible to mesh the simulation structure with milli-degree taper angle, parallel plate Fabry-Perot approximation was used. As shown in Fig 3, DBR – resonant gap – DBR is simulated. The increase in the number of [*HL*] pairs from [*HL*] to [*HLHLHLH*] to improve the full width half maximum (FWHM) but at the expense of attenuated transmission %. Fig 3 (inset) shows the FDTD simulation setup using [*HLH*] – resonant gap – [*HLH*] as example.

Some works on silicon-based thin film liftoff had been reported previously. Most of these thin films were done by reactive sputtering at low temperature. For example, Lee *et al*, reported on a successful liftoff of low temperature CVD deposited silicon nitride (40 nm) [32]. So far, only sub-micron thin silicon nitride film liftoff was reported [33]. In this work, we reported on a liftoff process for the deposition of thick micrometer height SiO_2 pillars (1.5 and 2.5 μm) by O_2 plasma. O_2 plasma is preferred as the dry process would not leave a film residue during stripping that could interfere with spectroscopic measurements later. To strip the photoresist

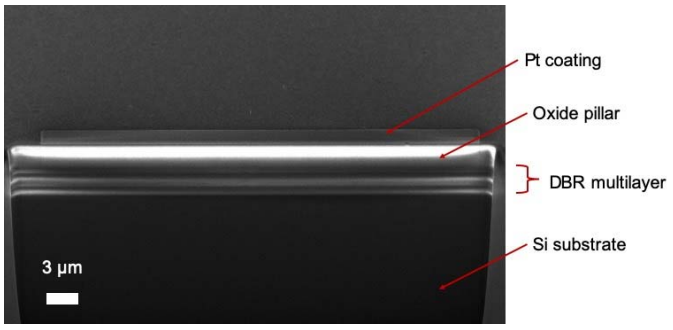

Fig. 4. Shows a cross-section side profile of a portion of a SiO_2 pillar as well as the revelation of the underlying DBR layers.

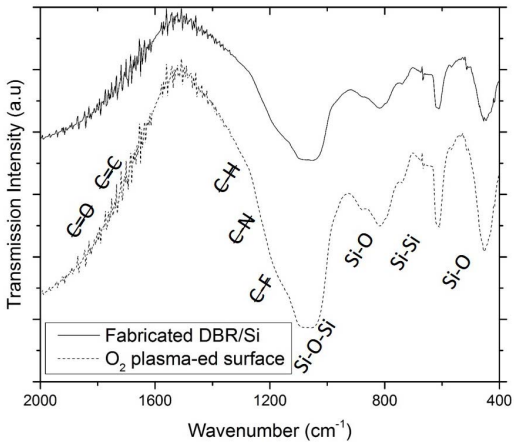

Fig. 5. Shows the fingerprint infrared spectra of as-deposited DBR on Si and B) DBR surface subjected to PR spin coating for SiO2 deposition and O2 plasma removal treatment. Some molecular species were intentionally crossed out to indicate their absence.

away, O_2 plasma was used twice as the resist was significantly hardened during SiO_2 deposition. Further cleaning is needed to remove stubborn polymeric residues, if any persists. The residues are a results of photoresist hardening when exposed to elevated temperature during the deposition of oxide pillars. Depending on the types of photoresists in use, process needs (such as achieving specific SiO_2 pillar height during HDCVD deposition), the resists might be thermally hardened to a different extent.

As illustrated in Fig 4, oxide pillar and underlying DBR layers were imaged. A Pt layer was deposited prior to the ion milling process during the FIB-SEM process. The main purpose of the Pt is to prevent the region of interest from ion beam induced artifacts. Furthermore, the Pt coating serves as a shield to preserves the morphology of the underlying structure during the milling process. FIB was performed on a 2.5 μm oxide pillar and was over etched into the Si substrate revealing the underlying DBR structure. The thickness corroborated with that of designed.

Transmission FTIR was performed on the sample before PR deposition as well as post-O_2 plasma stripping. The surface profile was compared to assess if there is a film of carbonized residue that could potentially introduce errors to actual data during optical measurement. As revealed in Fig 5, it can

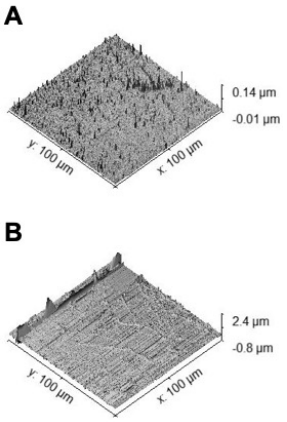

Fig. 6. Shows the A) surface topography of DBR deposited surface and B) DBR surface after O_2 plasma removal.

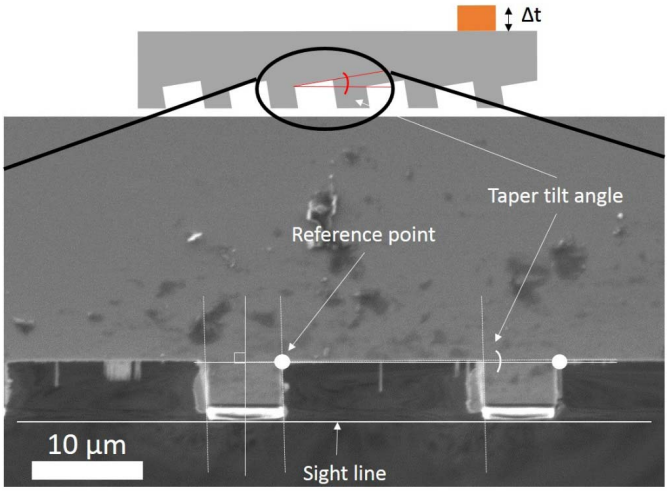

Fig. 7. Illustrates the concept of tilt etching to achieve a sloped angle of about 0.01° as determined by cross-sectional FESEM.

be observed that the peaks before and after O_2 plasma are strikingly similar. Those peaks present are attributed to Si-O-Si ($\sim$1100 cm^{-1}), Si-O (810 cm^{-1}), Si-Si (720 cm^{-1}) and Si-O (450 cm^{-1}) for the underlying DBR structures [34]. The reason why valleys were shown is because molecules which have strong resonant frequencies at those locations, absorb the incident light strongly, resulting in stronger attenuation of light. Thus, the transmitted signal, registered a lower response by the detector. The Si-O-Si peak presents at $\sim$1100 cm^{-1} could be due the presence of SiO_2. It had been reported by previous works [35], [36].

The absence of C-O, C-C, C-H, C-N and C-F peaks at 1725 - 1705, 1648 – 1638, 1385 – 1380, 1342 – 1266 and 1400 - 1000 cm^{-1}, respectively, conclude that the formation of oxide pillar and the DRIE etching processes do not introduce additional contaminants onto the DBR surfaces [37].

Tapping mode AFM was done to probe the surface topography of DBR top layer before PR deposition and after O_2 plasma treatment. Surface roughness (Rq) was measured to be 4.5 and 55.0 nm, respectively, as shown in Fig 6. The rougher post O_2 plasma surface is likely attributed to the presence of micro-clusters of yet to be removed leftover PR carbon residues. As revealed by the FTIR spectra in Fig 5, the presence of such clusters posed minimal effect to the performance of the component. On the other hand, it has been verified that the O_2 plasma process does not lead to the degradation of the DBR surface.

Despite that, almost all of the resists were removed as flakes when gently blown under a stream of dry N_2. As the HDCVD process temperature was performed at approximately 150 °C with the chuck temperature set to 18 °C, further lowerering of chuck temperature would ensure that the resist remains supple after deposition. This would render its removal easier. Furthermore, for future attempts of HDCVD deposition of SiO_2, PR that could withstand higher working temperature should be considered. On the other hand, a chemical cleaning method could be employed following that of ashing process [38].

For proper mating of the top and bottom substrates, holes were etched into the top wafer to accommodate the pillars. The main challenge is that the top wafer will have to be tilted at a milli-degree angle with respect to the bottom wafer. Therefore, the substrate is slanted at a similar angle during etching. Proper angle control was achieved by patterned resist on the backside of the wafer. When placed firmly on the DRIE chuck, the pillar would result in the required slant angle [39]. Subsequent DRIE etching allows the replication of angle as required. In this work, a total etch depth of approximately 300 nm was etched into the top-most layer of Si and etch stopped on the subsequent underlying SiO_2 layer. Unfortunately, due to the large pillar feature, it is not possible to observe the tilt at high magnification.

To properly visualize the concept of tilt etching, patterns with line and line spacing of 7.5 and 17.5 μm were deep etched for a depth of 4 μm. An optimized recipe that could reproduce highly vertical sidewall was used [40]. This enables one to observe the tilt angle at high magnification with greater ease. With reference to Fig 7, with a sightline as a horizontal reference, a tilt angle of $< 0.01°$ was measured. The obtained value corresponded to the desired taper angle.

Mated LVFs were subjected to FTIR optical transmission characterization. During testing, background reference was obtained in the air while the aperture was set to 100 μm $\times$ 100 μm. To measure the transmitted bands along the length of the filter, the sample stage was manually translated at interval steps of 100 μm. The transmitted passbands of the LVF can be seen in Fig 8A. It can be observed that the fabricated LVF possesses an optical stopband of 1.35 μm from 3.25 to 4.60 μm. Each coloured line indicates the transmission profile acquired along the length of the filter. During characterization, the filter was scanned from the end with the shorter resonant gap to the longer end. Correspondingly, transmission peaks with increasing wavelength are obtained as shown in Fig 8A. In particular, a FWHM of 230 nm was measured for the peak present at 3.5 μm. Simulated LVF passbands are shown in Fig 8B. The FWHM is approximated to be 220 nm. A narrower peak width can be obtained by increasing the number of DBR [HL] pair as illustrated in Fig 3.

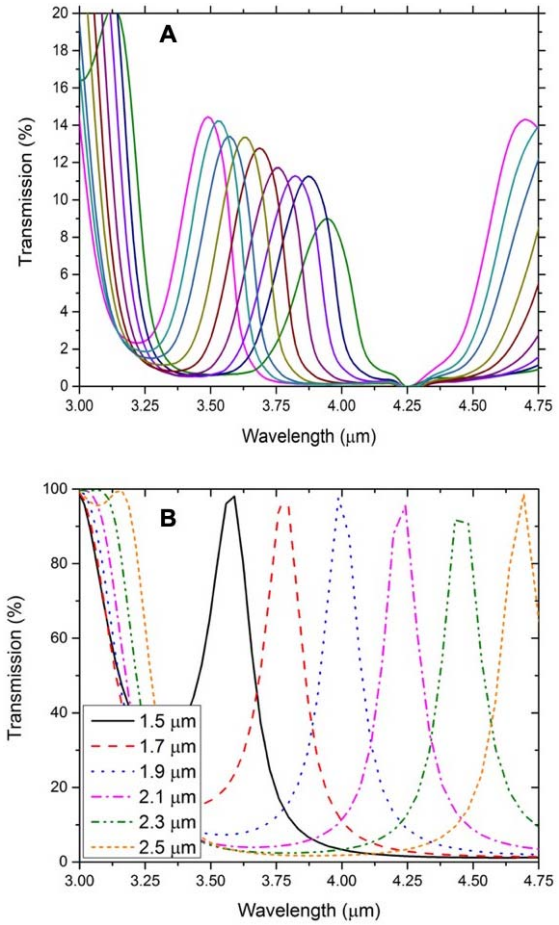

Fig. 8. A) shows the measured transmission profile of a mated LVF while B) shows the simulated transmission profile.

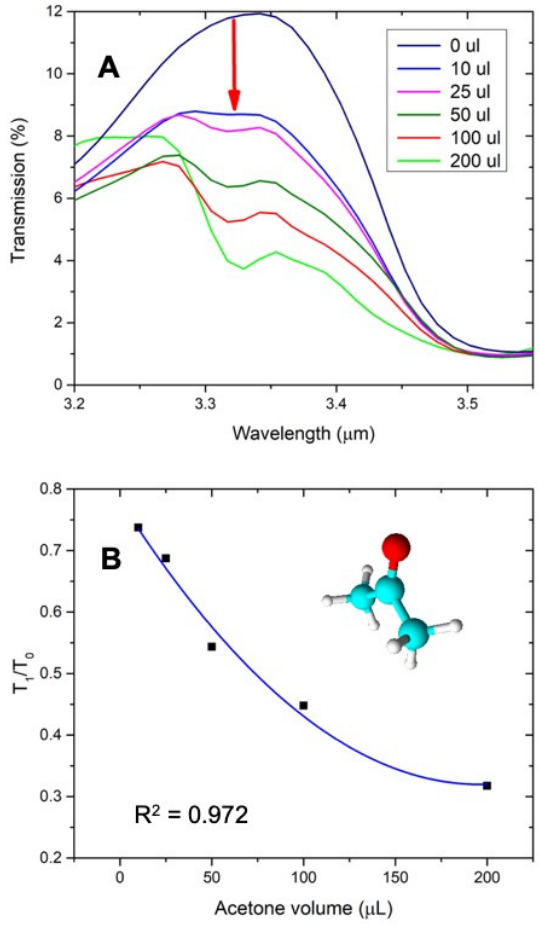

Fig. 9. Shows the A) transmission intensity attenuation by various acetone concentration, B) relationship between T_1/T_0 and acetone concentration. Inset is showing an acetone molecule ball and stick model.

The decrease in transmission between actual and simulated is attributed to light reflection and scattering at the air-Si wafer interface. Also, the small aperture used during testing resulted in partial attenuation of the incidental light intensity. Although the fabricated LVF has a delineated working range which is likely attributed to fabrication errors of the DBR, the working range is sufficient for C-H hydrocarbon detection.

The designed LVF is capable of hydrocarbon detection between 3.3 and 3.5 μm. To illustrate its performance, vaporized acetone was characterized in a glass gas cell. The single-pass cell was slotted in between the infrared source and the LVF. Prior to testing, a fresh background scan was taken in the presence of the empty cell. An amount of acetone was dispensed into the gas cell and heated to 80 °C. The measured optical response is shown in Fig 9A. It can be seen that the transmission % decreased strongly at 3.31 μm with an increase in acetone concentration.

A transmission ratio between attenuated transmission % (T_1) and the original peak intensity (T_0) was calculated. The plotted relationship between the transmission intensity ratio and acetone concentration is shown in Fig 9B. The fitted trend line has a correlation R^2 value of 0.972. The statistical test suggests good correlational characteristics between acetone concentration and (T_1/T_0) ratio. The superiority of a (T_1/T_0) ratio versus acetone concentration as compared to T% versus acetone concentration is that the data obtained from the former method is unaffected by variations in spectrometer parametric settings such as aperture size, light intensity, etc. For the latter, operation parameters have to be properly validated in order to compare data acquired during different run sessions fairly.

The reliability of the sensor performance is determined by the transmission profile of the passband. In this case, the transmission intensity and the full width half maximum (FWHM) are evaluated 6 months apart. It can be seen in Fig 10 that the passband peak intensity and (FWHM) at 3.33 μm, as denoted by S1-1 (before) and S1-1, are 11.9% (230 nm) and 11.55% (240 nm), respectively. The difference in transmission intensity is less than 3% while that of FWHM is about 4%. Although the LVF is stored at room temperature and pressure, the slight difference in performance suggests a highly reliable sensor construction. Accelerated reliability testing under high heat and humidity in the presence of acetone would be undertaken in the future.

To determine the accuracy, reproducibility and repeatability of this class of sensor, a total of 5 sensors were individually fabricated. Two sensors (S1 and S2) were optically characterized. Then, the transmission profiles at three separate locations along the breath (shown in Fig 10 inset) of the sensors

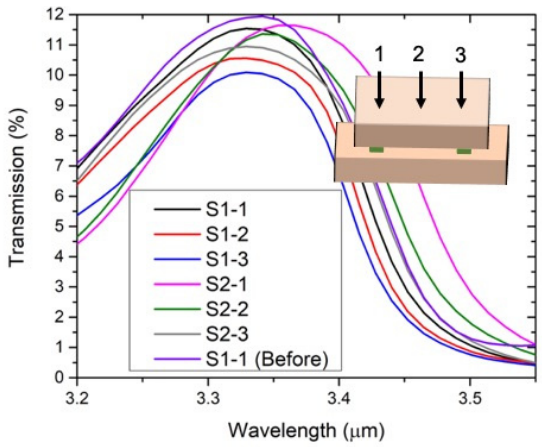

Fig. 10. Shows the transmission profile at 3.33 μm measured at different locations on 2 samples. Specifically, sample 1 is evaluated at location 1 approximately six months apart. The inset shows the side view of the breath of the LVF. The arrow-number indicates the position of optical response acquisition.

were optically probed for changes in intensity and FWHM. As observed in Fig 10, the calculated mean (standard deviation) and FWHM (standard deviation) are 11.14% (0.64%) and 230 nm (0.009 nm), respectively. The small spread in mean intensity depicts the stability of the deposited Bragg mirror in air. For an unstable system, as the surface degrades, the surface roughness increases, causing greater light scattering which would affect light transmission. FWHM is determined by the overall quality of the fabricated sensor. In this case, the low standard deviation in FWHM between the samples indicates that the entire fabrication process is well-controlled.

IV. Future Works

This work can be extended to simultaneous detection of different hydrocarbons with a proper setup of T_1/T_0. By altering the pillar height, height different (taper angle) and DBR [*HL*] materials, LVFs for different operating ranges and end uses can be fabricated.

To realize a mechanically robust and reliable LVF, the top and bottom substrates could be wafer bonded together. In this case, the use of metal-metal thermocompression, eutectic bonding or low temperature Si-O-Si fusion bonding is proposed [41], [42]. The bonding interface would be the interfaces between the etched holes and the HDCVD SiO_2 pillars. A better bonding experience can be set up by including a graphite padding to compensate for the height gradient along the length of the LVF. On the other hand, although not demonstrated in this work, the presented LVF can be extended to the construction of a hyperspectral imaging filter. To achieve that, supporting pillars of a two-dimensional square filter are fabricated with different oxide pillar heights resulting in a two axes tilt.

In addition, the concept of oxide deposition presented in this work could possibly be used to create silicon-on-insulator (SOI) on selected areas for applications in silicon photonics as well as non-conductive bump support for three-dimension integrated circuits (3DIC).

V. Conclusion

The construction of a normal incidence LVF using oxide pillars is presented and characterized. The oxide pillars, fabricated with photoresists and liftoff, provide a sandwich to create an air gap resonator. In addition, the difference in pillar height ($t_1 - t_2$) can be used to manipulate the taper angle during etching. The constructed mid-infrared responsive LVF, with a operating range from 3.25 – 4.60 μm, is capable of hydrocarbon detection between 3.3 and 3.5 μm. Hydrocarbon detection is demonstrated with acetone level monitoring between 10 and 200 μl. By taking the transmission intensity ratio, T_1/T_0, a parameter-independent normalized ratio between transmission and analyte concentration is obtained. Finally, R^2 of 0.972 for T_1/T_0 versus acetone volume, is achieved in this work.

Acknowledgment

The author S. C. K. Goh would like to thank Economic Development Board of Singapore (EDB) and Excelitas Technologies for the Industrial Postgraduate (IPP) Scholarship.

References

[1] A. D. Wilson, "Review of electronic-nose technologies and algorithms to detect hazardous chemicals in the environment," *Procedia Technol.*, vol. 1, pp. 453–463, Jan. 2012.
[2] J. Zhu *et al.*, "Development trends and perspectives of future sensors and MEMS/NEMS," *Micromachines*, vol. 11, no. 1, p. 7, Dec. 2019.
[3] H.-C. Park, J.-H. Lee, S.-G. Park, D.-S. Yee, and K.-H. Jeong, "Millimeter scale electrostatic mirror with sub-wavelength holes for terahertz wave scanning," *Appl. Phys. Lett.*, vol. 102, no. 3, Jan. 2013, Art. no. 031111.
[4] M. Akbar, M. Restaino, and M. Agah, "Chip-scale gas chromatography: From injection through detection," *Microsyst. Nanoeng.*, vol. 1, no. 1, p. 15039, Dec. 2015.
[5] K.-S. Shin, S. K. Kim, E. G. Yang, T. S. Kim, J. Y. Kang, and J. H. Park, "Miniaturized fluorescence detection chip for queching assay of Atrazine," in *Proc. 5th IEEE Conf. Sensors*, Oct. 2006, pp. 366–369.
[6] R. Szedlak *et al.*, "Remote sensing with commutable monolithic laser and detector," *ACS Photon.*, vol. 3, no. 10, pp. 1794–1798, Oct. 2016.
[7] H. Wang *et al.*, "Source profiles and chemical reactivity of volatile organic compounds from solvent use in Shanghai, China," *Aerosol Air Qual. Res.*, vol. 14, no. 1, pp. 301–310, 2014.
[8] R. Atkinson and J. Arey, "Atmospheric degradation of volatile organic compounds," *Chem. Rev.*, vol. 103, no. 12, pp. 4605–4638, Dec. 2003.
[9] G. St. Helen, P. Jacob, M. Peng, D. A. Dempsey, S. K. Hammond, and N. L. Benowitz, "Intake of toxic and carcinogenic volatile organic compounds from secondhand smoke in motor vehicles," *Cancer Epidemiol. Biomarkers Prevention*, vol. 23, no. 12, pp. 2774–2782, Dec. 2014.
[10] T. Jin, J. Zhou, and P. T. Lin, "Mid-infrared waveguides for volatile organic compounds detection," in *Proc. Opt. Sensors Sens. Congr.*, San Jose, CA, USA, 2019.
[11] J.-S. Lee *et al.*, "Volatile organic compounds optical fiber gas sensor based on evanescentl field coupling and solvatochromism," in *Proc. IEEE SENSORS*, Nov. 2013, pp. 1–4.
[12] K. Kanda and T. Maekawa, "Development of a WO_3 thick-film-based sensor for the detection of VOC," *Sens. Actuators B, Chem.*, vol. 108, nos. 1–2, pp. 97–101, Jul. 2005.
[13] Y. H. Kim *et al.*, "Self–activated transparent all–graphene gas sensor with endurance to humidity and mechanical bending," *ACS Nano*, vol. 9, no. 10, pp. 10453–10460, Oct. 2015.
[14] L. Zhao *et al.*, "Room temperature formaldehyde sensing of hollow SnO_2/ZnO heterojunctions under UV–LED activation," *IEEE Sensors J.*, vol. 19, no. 17, pp. 7207–7214, Sep. 2019.
[15] K. Liu, Y. Cao, G. Wang, W. Zhang, W. Chen, and X. Gao, "A novel photoacoustic spectroscopy gas sensor using a low cost polyvinylidene fluoride film," *Sens. Actuators B, Chem.*, vol. 277, pp. 571–575, Dec. 2018.

[16] S. Pevec and D. Donlagic, "Miniature fiber-optic Fabry–Pérot refractive index sensor for gas sensing with a resolution of 5×10^9 RIU," *Opt. Express*, vol. 26, no. 18, p. 23868, Sep. 2018.

[17] T. Hemati and B. Weng, "The mid-infrared photonic crystals for gas sensing applications," *Photonic Cryst. Glimpse Current Res. Trends*, Feb. 2019.

[18] Z. Wang *et al.*, "Single-shot on-chip spectral sensors based on photonic crystal slabs," *Nature Commun.*, vol. 10, no. 1, p. 1020, Dec. 2019.

[19] L. P. Schuler, J. S. Milne, J. M. Dell, and L. Faraone, "MEMS-based microspectrometer technologies for NIR and MIR wavelengths," *J. Phys. D, Appl. Phys.*, vol. 42, no. 13, Jul. 2009, Art. no. 133001.

[20] P. H. Cu-Nguyen, Z. Wang, and H. Zappe, "Concepts for compact mid-IR spectroscopy in photochemistry," *Proc. SPIE*, vol. 10025, Nov. 2016, Art. no. 100251O.

[21] M. Dami *et al.*, "Ultra compact spectrometer using linear variable filters," *Proc. SPIE*, vol. 10565, Jan. 2018, Art. no. 1056559.

[22] A. Piegari, A. K. Sytchkova, I. D. Sarcina, and J. Bulir, "Visible and near-infrared filters for miniaturized spectrometers," *Proc. SPIE, Astronomical Telescopes Instrum.*, vol. 7018, Jul. 2008, Art. no. 701855.

[23] L. Abel-Tiberini, F. Lemarquis, G. Marchand, L. Roussel, G. Albrand, and M. Lequime, "Manufacturing of linear variable filters with straight iso-thickness lines," *Proc. SPIE Opt. Syst. Des.*, vol. 5963, Oct. 2005, Art. no. 59630B.

[24] K. Du, J. Ding, Y. Liu, I. Wathuthanthri, and C.-H. Choi, "Stencil lithography for scalable micro- and nanomanufacturing," *Micromachines*, vol. 8, no. 4, p. 131, Apr. 2017.

[25] S. Zhang *et al.*, "Mixed-gas $CH_4/CO_2/CO$ detection based on linear variable optical filter and thermopile detector array," *Nanoscale Res. Lett.*, vol. 14, no. 1, p. 348, Dec. 2019.

[26] S. Saxe *et al.*, "Advances in miniaturized spectral sensors," *Proc. SPIE Commercial Sci. Sens. Imag.*, vol. 10657, May 2018, Art. no. 106570B.

[27] A. Emadi, H. Wu, S. Grabarnik, G. De Graaf, and R. F. Wolffenbuttel, "Vertically tapered layers for optical applications fabricated using resist reflow," *J. Micromech. Microeng.*, vol. 19, no. 7, Jul. 2009, Art. no. 074014.

[28] N. P. Ayerden and R. F. Wolffenbuttel, "How accurate is the Fabry–Pérot approximation in high-finesse linear variable optical filters for gas absorption spectroscopy?" in *Proc. 19th Int. Conf. Solid-State Sens., Actuators Microsyst. (TRANSDUCERS)*, Jun. 2017, pp. 2111–2114.

[29] C. F. Mateus, M. C. Huang, and C. J. Chang-Hasnain, "Micromechanical tunable optical filters: General design rules for wavelengths from near-IR up to 10 μm," *Sens. Actuators A, Phys.*, vol. 119, no. 1, pp. 57–62, Mar. 2005.

[30] N. P. Ayerden, G. De Graaf, and R. F. Wolffenbuttel, "Compact gas cell integrated with a linear variable optical filter," *Opt. Express*, vol. 24, no. 3, p. 2981, Feb. 2016.

[31] *Lumerical: High-Performance Photonic Simulation Software*. Accessed: Jul. 31, 2019. [Online]. Available: https://www.lumerical.com

[32] J. Y.-M. Lee, M. M. Dange, and K. Sooriakumar, "A novel lift-off process using low-temperature PECVD silicon nitride for the fabrication of self-aligned gate GaAs MESFETs and InP MISFETs," *Microelectron. Eng.*, vol. 18, no. 3, pp. 215–223, Aug. 1992.

[33] E. Vanhove, A. Tsopéla, L. Bouscayrol, A. Desmoulin, J. Launay, and P. Temple-Boyer, "Final capping passivation layers for long-life microsensors in real fluids," *Sens. Actuators B, Chem.*, vol. 178, pp. 350–358, Mar. 2013.

[34] Y. Peng, J. Zhou, X. Zheng, B. Zhao, and X. Tan, "Structure and photoluminescence properties of silicon oxycarbide thin films deposited by the RF reactive sputtering," *Int. J. Mod. Phys. B*, vol. 25, no. 22, pp. 2983–2990, Sep. 2011.

[35] T. N. Tran, T. V. A. Pham, M. L. P. Le, T. P. T. Nguyen, and V. M. Tran, "Synthesis of amorphous silica and sulfonic acid functionalized silica used as reinforced phase for polymer electrolyte membrane," *Adv. Nat. Sci, Nanosci. Nanotechnol.*, vol. 4, no. 4, Sep. 2013, Art. no. 045007.

[36] S. Dirè, G. Facchin, R. Ceccato, L. Guarino, A. Sassi, and M. Gleria, "Hydroxylated cyclophosphazene/silica hybrid materials: Synthesis and characterization," *J. Inorganic Organometallic Polym.*, vol. 12, no. 3, pp. 59–78, Dec. 2002.

[37] S. Rimal *et al.*, "Interfacial characterization of post-etch polymer residues and plasma treated Cu surfaces related to advanced Cu interconnects," in *Proc. SEMICON Korea*, Dec. 2012.

[38] G. G. Totir *et al.*, "Post ion-implant photoresist removal via wet chemical cleans combined with physical force pretreatments," *ECS Trans.*, vol. 11, pp. 219–226, Sep. 2007.

[39] Y. C. Lien, S. H. Chen, E. Yi-Chang, C. T. Lee, L. Chu, and C.-Y. Chang, "Fabrication of 0.15-μm Γ-shaped gate $In_{0.52}/Al_{0.48}/As/In_{0.6}/Ga_{0.4}/as$ metamorphic HEMTs using DUV lithography and tilt dry-etching technique," *IEEE Electron Device Lett.*, vol. 28, no. 2, pp. 93–95, Mar. 2007.

[40] S. C. K. Goh, N. Chen, L. L. Shiau, B. K. Tay, C. Lee, and C. S. Tan, "Deposited poly-Si as on-demand linewidth compensator for on-chip Fabry–Pérot interferometer and vertical linear variable optical filter bandpass and passband manipulation," *J. Micromech. Microeng.*, vol. 29, no. 4, Apr. 2019, Art. no. 047001.

[41] S. L. Chua, J. M. Chan, S. C. K. Goh, and C. S. Tan, "Cu–Cu bonding in ambient environment by Ar/N_2 plasma surface activation and its characterization," *IEEE Trans. Compon., Packag. Manuf., Technol.*, vol. 9, no. 3, pp. 596–605, Mar. 2019.

[42] N. Quack, S. Han, and M. C. Wu, "Wafer level AlGe eutectic bonding for MEMS-electronic-photonic heterogeneous integration," in *Proc. Int. Nano-Optoelectron. Workshop*, Aug. 2012.